Title

Wavefront sensorless adaptive optics fluorescence biomicroscope for in vivo retinal imaging in mice

Journal

Biomedical Optics Express, 7(1)

ISSN

2156-7085

Authors

Wahl, Daniel J
Jian, Yifan
Bonora, Stefano
et al.

Publication Date

2016

DOI

10.1364/boe.7.000001

Peer reviewed

Biomedical Optics EXPRESS

Wavefront sensorless adaptive optics fluorescence biomicroscope for *in vivo* retinal imaging in mice

Daniel J. Wahl,[1,6] Yifan Jian,[1,6] Stefano Bonora,[2,3] Robert J. Zawadzki,[4,5] and Marinko V. Sarunic[1,*]

[1]*Engineering Science, Simon Fraser University, Burnaby BC, V5A 1S6 Canada*
[2]*CNR-Institute for Photonics and Nanotechnology, Via Trasea 7, 35131, Padova, Italy*
[3]*Hilase project, Institute of Physics AS CR v.v.i., Na Slovance 2, 18221, Prague, Czech Republic*
[4]*UC Davis RISE Small Animal Ocular Imaging Facility, Department of Cell Biology and Human Anatomy, University of California Davis, Davis, CA 95616 USA*
[5]*Vision Science and Advanced Retinal Imaging Laboratory (VSRI), Department of Ophthalmology & Vision Science, University of California Davis, Sacramento, CA 95817 USA*
[6]*These authors contributed equally to this work.*
[*]*msarunic@sfu.ca*

Abstract: Cellular-resolution *in vivo* fluorescence imaging is a valuable tool for longitudinal studies of retinal function in vision research. Wavefront sensorless adaptive optics (WSAO) is a developing technology that enables high-resolution imaging of the mouse retina. In place of the conventional method of using a Shack-Hartmann wavefront sensor to measure the aberrations directly, WSAO uses an image quality metric and a search algorithm to drive the shape of the adaptive element (i.e. deformable mirror). WSAO is a robust approach to AO and it is compatible with a compact, low-cost lens-based system. In this report, we demonstrated a hill-climbing algorithm for WSAO with a variable focus lens and deformable mirror for non-invasive *in vivo* imaging of EGFP (enhanced green fluorescent protein) labelled ganglion cells and microglia cells in the mouse retina.

OCIS codes: (170.4460) Ophthalmic optics and devices; (010.1080) Active or adaptive optics; (170.0110) Imaging systems; (170.4470) Ophthalmology.

References and links

1. Y. Geng, A. Dubra, L. Yin, W. H. Merigan, R. Sharma, R. T. Libby, and D. R. Williams, "Adaptive optics retinal imaging in the living mouse eye," Biomed. Opt. Express **3**(4), 715–734 (2012).
2. J. Schallek, Y. Geng, H. Nguyen, and D. R. Williams, "Morphology and topography of retinal pericytes in the living mouse retina using in vivo adaptive optics imaging and ex vivo characterization," Invest. Ophthalmol. Vis. Sci. **54**(13), 8237–8250 (2013).
3. B. C. Chauhan, K. T. Stevens, J. M. Levesque, A. C. Nuschke, G. P. Sharpe, N. O'Leary, M. L. Archibald, and X. Wang, "Longitudinal in vivo imaging of retinal ganglion cells and retinal thickness changes following optic nerve injury in mice," PLoS One **7**(6), e40352 (2012).
4. L. Chen, P. Yang, and A. Kijlstra, "Distribution, markers, and functions of retinal microglia," Ocul. Immunol. Inflamm. **10**(1), 27–39 (2002).
5. P. Zhang, A. Zam, Y. Jian, X. Wang, M. E. Burns, M. V. Sarunic, E. N. Pugh, and R. J. Zawadzki, "Multispectral scanning laser ophthalmoscopy combined with optical coherence tomography for simultaneous in vivo mouse retinal imaging," Proc. SPIE **9307**, 93070H (2015).
6. C. Alt, J. M. Runnels, L. J. Mortensen, W. Zaher, and C. P. Lin, "In vivo imaging of microglia turnover in the mouse retina after ionizing radiation and dexamethasone treatment," Invest. Ophthalmol. Vis. Sci. **55**(8), 5314–5319 (2014).
7. Y. Geng, L. A. Schery, R. Sharma, A. Dubra, K. Ahmad, R. T. Libby, and D. R. Williams, "Optical properties of the mouse eye," Biomed. Opt. Express **2**(4), 717–738 (2011).
8. D. R. Williams, "Imaging single cells in the living retina," Vision Res. **51**(13), 1379–1396 (2011).
9. A. Roorda, "Adaptive optics for studying visual function: a comprehensive review," J. Vis. **11**(5), 6 (2011).

#246171 Received 30 Jul 2015; revised 15 Oct 2015; accepted 21 Oct 2015; published 4 Dec 2015

10. J. Porter, H. Queener, J. Lin, K. Thorn, and A. Awwal, *Adaptive Optics for Vision Science: Principles, Practices, Design and Applications* (Wiley, 2006).
11. R. Tyson, *Principles of Adaptive Optics* (CRC Press, 2010).
12. J. A. Kubby, *Adaptive Optics for Biological Imaging* (CRC Press, 2013).
13. R. J. Zawadzki, P. Zhang, A. Zam, E. B. Miller, M. Goswami, X. Wang, R. S. Jonnal, S. H. Lee, D. Y. Kim, J. G. Flannery, J. S. Werner, M. E. Burns, and E. N. Pugh, Jr., "Adaptive-optics SLO imaging combined with widefield OCT and SLO enables precise 3D localization of fluorescent cells in the mouse retina," Biomed. Opt. Express **6**(6), 2191–2210 (2015).
14. Y. N. Sulai and A. Dubra, "Non-common path aberration correction in an adaptive optics scanning ophthalmoscope," Biomed. Opt. Express **5**(9), 3059–3073 (2014).
15. J. W. Evans, R. J. Zawadzki, S. M. Jones, S. S. Olivier, and J. S. Werner, "Error budget analysis for an Adaptive Optics Optical Coherence Tomography System," Opt. Express **17**(16), 13768–13784 (2009).
16. F. Felberer, J. S. Kroisamer, C. K. Hitzenberger, and M. Pircher, "Lens based adaptive optics scanning laser ophthalmoscope," Opt. Express **20**(16), 17297–17310 (2012).
17. A. Dubra and Y. Sulai, "Reflective afocal broadband adaptive optics scanning ophthalmoscope," Biomed. Opt. Express **2**(6), 1757–1768 (2011).
18. M. J. Booth, "Adaptive optics in microscopy," Philos. Trans. A Math Phys. Eng. Sci. **365**(1861), 2829–2843 (2007).
19. Y. Jian, R. J. Zawadzki, and M. V. Sarunic, "Adaptive optics optical coherence tomography for in vivo mouse retinal imaging," J. Biomed. Opt. **18**(5), 056007 (2013).
20. K. S. K. Wong, Y. Jian, M. Cua, S. Bonora, R. J. Zawadzki, and M. V. Sarunic, "In vivo imaging of human photoreceptor mosaic with wavefront sensorless adaptive optics optical coherence tomography," Biomed. Opt. Express **6**(2), 580–590 (2015).
21. Y. Jian, J. Xu, M. A. Gradowski, S. Bonora, R. J. Zawadzki, and M. V. Sarunic, "Wavefront sensorless adaptive optics optical coherence tomography for in vivo retinal imaging in mice," Biomed. Opt. Express **5**(2), 547–559 (2014).
22. D. P. Biss, D. Sumorok, S. A. Burns, R. H. Webb, Y. Zhou, T. G. Bifano, D. Côté, I. Veilleux, P. Zamiri, and C. P. Lin, "In vivo fluorescent imaging of the mouse retina using adaptive optics," Opt. Lett. **32**(6), 659–661 (2007).
23. C. Alt, D. P. Biss, N. Tajouri, T. C. Jakobs, and C. P. Lin, "An adaptive-optics scanning laser ophthalmoscope for imaging murine retinal microstructure," Proc. SPIE **7550**, 755019 (2010).
24. L. Yin, Y. Geng, F. Osakada, R. Sharma, A. H. Cetin, E. M. Callaway, D. R. Williams, and W. H. Merigan, "Imaging light responses of retinal ganglion cells in the living mouse eye," J. Neurophysiol. **109**(9), 2415–2421 (2013).
25. R. Sharma, L. Yin, Y. Geng, W. H. Merigan, G. Palczewska, K. Palczewski, D. R. Williams, and J. J. Hunter, "In vivo two-photon imaging of the mouse retina," Biomed. Opt. Express **4**(8), 1285–1293 (2013).
26. S. A. Burns, R. Tumbar, A. E. Elsner, D. Ferguson, and D. X. Hammer, "Large-field-of-view, modular, stabilized, adaptive-optics-based scanning laser ophthalmoscope," J. Opt. Soc. Am. A **24**(5), 1313–1326 (2007).
27. M. Martínez-Corral, A. Doblas, E. Sánchez-Ortiga, J. Sola-Pikabea, and G. Saavedr, "Static real-time capture of 3D microscopy images," in SPIE Newsroom, https://spie.org/x113256.xml (2015).
28. L. N. Thibos, R. A. Applegate, J. T. Schwiegerling, and R. Webb; VSIA Standards Taskforce Members. Vision science and its applications, "Standards for reporting the optical aberrations of eyes," J. Refract. Surg. **18**(5), S652–S660 (2002).
29. A. Myronenko and X. Song, "Intensity-based image registration by minimizing residual complexity," IEEE Trans. Med. Imaging **29**(11), 1882–1891 (2010).
30. A. Dubra and Z. Harvey, "Registration of 2D Images from Fast Scanning Ophthalmic Instruments," in *Biomedical Image Registration*, Vol. 6204 of Lecture Notes in Computer Science (Springer, Berlin), pp. 60–71 (2010).
31. C. K. Sheehy, Q. Yang, D. W. Arathorn, P. Tiruveedhula, J. F. de Boer, and A. Roorda, "High-speed, image-based eye tracking with a scanning laser ophthalmoscope," Biomed. Opt. Express **3**(10), 2611–2622 (2012).
32. O. P. Kocaoglu, R. D. Ferguson, R. S. Jonnal, Z. Liu, Q. Wang, D. X. Hammer, and D. T. Miller, "Adaptive optics optical coherence tomography with dynamic retinal tracking," Biomed. Opt. Express **5**(7), 2262–2284 (2014).
33. W. Sun, N. Li, and S. He, "Large-scale morphological survey of mouse retinal ganglion cells," J. Comp. Neurol. **451**(2), 115–126 (2002).
34. J. Coombs, D. van der List, G. Y. Wang, and L. M. Chalupa, "Morphological properties of mouse retinal ganglion cells," Neuroscience **140**(1), 123–136 (2006).
35. W. Zou, X. Qi, and S. A. Burns, "Wavefront-aberration sorting and correction for a dual-deformable-mirror adaptive-optics system," Opt. Lett. **33**(22), 2602–2604 (2008).
36. C. Li, N. Sredar, K. M. Ivers, H. Queener, and J. Porter, "A correction algorithm to simultaneously control dual deformable mirrors in a woofer-tweeter adaptive optics system," Opt. Express **18**(16), 16671–16684 (2010).
37. S. M. Jones, S. Olivier, D. Chen, S. Joeres, S. Sadda, R. J. Zawadzki, J. S. Werner, and D. T. Miller, "Adaptive optics ophthalmologic systems using dual deformable mirrors," Proc. SPIE **6467**, 64670H (2007).
38. X. Zhou, P. Bedggood, and A. Metha, "Limitations to adaptive optics image quality in rodent eyes," Biomed. Opt. Express **3**(8), 1811–1824 (2012).

#246171 Received 30 Jul 2015; revised 15 Oct 2015; accepted 21 Oct 2015; published 4 Dec 2015

39. S. Zommer, E. N. Ribak, S. G. Lipson, and J. Adler, "Simulated annealing in ocular adaptive optics," Opt. Lett. **31**(7), 939–941 (2006).
40. H. Hofer, N. Sredar, H. Queener, C. Li, and J. Porter, "Wavefront sensorless adaptive optics ophthalmoscopy in the human eye," Opt. Express **19**(15), 14160–14171 (2011).
41. G. Palczewska, Z. Dong, M. Golczak, J. J. Hunter, D. R. Williams, N. S. Alexander, and K. Palczewski, "Noninvasive two-photon microscopy imaging of mouse retina and retinal pigment epithelium through the pupil of the eye," Nat. Med. **20**(7), 785–789 (2014).
42. Y. Geng, K. P. Greenberg, R. Wolfe, D. C. Gray, J. J. Hunter, A. Dubra, J. G. Flannery, D. R. Williams, and J. Porter, "In vivo imaging of microscopic structures in the rat retina," Invest. Ophthalmol. Vis. Sci. **50**(12), 5872–5879 (2009).
43. S. Bonora, Y. Jian, P. Zhang, A. Zam, E. N. Pugh, R. J. Zawadzki, and M. V. Sarunic, "Wavefront correction and high-resolution in vivo OCT imaging with an objective integrated multi-actuator adaptive lens," Opt. Express **23**(17), 21931–21941 (2015).

1. Introduction

Small animal models of diseases are a vital component in vision research because they facilitate the understanding of underlying biological processes, the identification of potential causative genes for human disorders, and the development of therapies against vision-robbing diseases. Mice are commonly used for preclinical vision research due to the significant anatomical and functional similarity of their eyes to human eyes and to the availability of transgenic strains that model human diseases. Non-invasive *in vivo* retinal imaging has the potential to reduce the number of animals required for a study, which in turn reduces the development time and the cost of new therapies [1]. Transgenic mice expressing endogenous fluorescent markers, such as Enhanced Green Fluorescent Protein (EGFP), are particularly important for vision research. The ability to image molecular markers has the potential to accelerate vision research by allowing retinal function to be observed *in vivo* and by permitting longitudinal studies of the same animal [2]. Research animals expressing EGFP in neuronal cells, including retinal ganglion cells and axons, are useful for studying retinal neurodegenerative diseases such as glaucoma [3]. Similarly, mice with EGFP-labelled microglia enable the *in vivo* study of the retinal response to diabetic retinopathy, glaucoma, and age-related macular degeneration [4–6]. Additional examples of vision research based on fluorescence imaging are described in Zhang *et al.* [5], and Alt *et al.* [6], just to name a few. Non-invasive fluorescence imaging of the mouse retina with even higher resolution is desirable, but requires correction of optical aberrations in the mouse eye [7].

Adaptive optics (AO) for ophthalmoscopy is an important tool for ophthalmologists and vision scientists, permitting cellular-resolution imaging of the retina. For non-invasive *in vivo* imaging in humans, AO has been demonstrated to improve the resolution for fundus photography, scanning laser ophthalmoscopy (SLO), and optical coherence tomography (OCT); there are several reviews on this topic, including [8–12]. The geometry of the mouse eye allows for focusing light on the retina with a higher numerical aperture (NA) than in humans, which allows for even higher resolution imaging *in vivo*. Due to the higher NA, the mouse eye is even more sensitive to aberrations induced when imaging with a large diameter beam, with aberrations introduced from the ocular tissues (i.e. cornea, lens and vitreous humour) [7]. AO facilitates retinal imaging with diffraction-limited performance at cellular resolution in mice.

Conventional AO compensates for aberrations in the wavefront with an adaptive element such as a deformable mirror (DM) controlled by a Shack-Hartmann (SH) wavefront sensor (WFS) in a closed feedback loop. The common approach of wavefront sensing is to use an extra light source (beacon) with low NA to measure the wavefront aberrations with the SH-WFS [1, 12, 13]. However, the beacon adds to the limited optical power that is allowed into the eye and contributes to non-common path errors [14]. The ability of the WFS-based AO system to correct wavefront aberrations can be limited by the WFS design (its accuracy and dynamic range) and a geometry mismatch between the WFS and the adaptable element, leading to wavefront correction errors [15]. The SH-WFS performance is also susceptible to

#246171 Received 30 Jul 2015; revised 15 Oct 2015; accepted 21 Oct 2015; published 4 Dec 2015

specular reflection from lenses and optical elements within the system [16]. Many of these issues have been addressed in different ways with AO system modifications. For example, efficient spherical mirror-based telescopes can be implemented to maintain signal and minimize back-reflections into the SH-WFS [17]. More compact AO systems have been developed with lens-based optics and polarizing elements to reduce these back-reflections [16]. For applications in vision science and small animal retinal imaging, a SH-WFS is further hampered by the 'small eye artifact', in which multiple reflecting/backscattering surfaces in the retina affect the wavefront measurement [7].

Some of the challenges associated with the SH-WFS can be better managed through Wavefront Sensorless Adaptive Optics (WSAO), which uses information from the quality of the image to guide aberration correction. Wavefront sensorless techniques have been applied in microscopy [18] and ophthalmic imaging for both human and mouse eyes [19–21].

In this paper, we expand on our previous work combining WSAO with Fourier-domain OCT for mouse retinal imaging, and present fluorescence images of mouse retina. AO fluorescence retinal imaging in mice has been presented with different modalities and methods throughout the Literature [1, 2, 13, 22–25], including both with and without a WFS. Notably, WFS-AO for *in vivo* subcellular-resolution imaging has been presented using an annular beam for the beacon, a high-resolution SH-WFS, and a mirror-based optical system [1, 2, 13]. We have implemented a lens-based WSAO system with a modal hill-climbing optimization algorithm using fluorescent image intensity as a metric. We used the combination of a variable focus lens and a small-stroke MEMS (microelectromechanical system) deformable mirror to perform defocus and aberration correction in the mouse eyes. The details of the experimental methods are described in the next section. The system performance was evaluated on phantoms, and representative images acquired from mouse retina *in vivo* are presented. Our results demonstrate that AO can be simple and compact with cellular resolution.

2. Methods

We have implemented a compact and low-cost confocal biomicroscope in order to acquire both reflectance (structural) and fluorescence (functional) images from mouse retina simultaneously. The system used off-the-shelf lenses with a smaller footprint and simpler design compared to the AO configurations that are based on SH-WFS and constructed from curved mirrors. A benefit of the lens-based system is that it permits a relatively wide field of view (FOV) to be imaged on the mouse retina [16, 26], albeit without diffraction-limited imaging performance outside of the isoplanatic patch. The wide field structural image was used in real-time to navigate on the retina using features such as blood vessels and the optic nerve head. Once centered at the desired location using a FOV of about 0.8 mm, the FOV was reduced to 0.2 mm or smaller for acquisition of the high-resolution fluorescence images that are presented below.

During imaging, the mouse was aligned to the imaging system using a plano-concave 'fundus lens,' with a 2 mm contact diameter and no magnification (Volk Optical Inc, Mentor, OH) that canceled out most of the refractive power from the mouse cornea; we utilized an external objective to focus the light on the mouse retina. For this reason, we refer to the imaging system as a fluorescence confocal (f/c) biomicroscope rather than an ophthalmoscope. The fundus lens approach to retinal imaging has several benefits: it facilitates alignment of the mouse, provides mechanical stability, and retains the moisture of the mouse cornea during imaging.

2.1 Mouse handling

The two strains of EGFP-labelled mice, B6.Cg-Tg(Thy1-EGFP)MJrs/J (ganglion cells) and B6.129P-Cx3cr1^{tm1Litt}/J (microglia cells), that were imaged in this report were obtained from Jackson Laboratories (Bar Harbor, ME). The mouse imaging sessions were performed under

#246171 Received 30 Jul 2015; revised 15 Oct 2015; accepted 21 Oct 2015; published 4 Dec 2015

protocols compliant to the Canadian Council on Animal Care, and with the approval of the University Animal Care Committee at Simon Fraser University. Prior to the imaging experiment, the mice were anesthetized with a subcutaneous injection of ketamine (100 mg/kg of body weight) and dexmedetomidine (0.1 mg/kg of body weight). Next, the eyes were dilated with a drop of topical solution (Tropicamide, 1%) and a couple minutes later, a drop of topical anesthetic (Alcaine, 0.5%) was applied. Artificial tear gel (Alcon, Fort Worth, TX) was applied liberally to protect the cornea from dehydration. The anesthetized mouse was placed on a translation stage and the eye was gently aligned with direct contact to the fundus lens. The laser power at the fundus lens was ~150 µW. The mice were recovered after the experiment using atipamezole injected at 1.8 mg/kg of body weight. The local anesthetic was applied to reduce potential irritation to the mouse after recovery due to the contact with the fundus lens.

2.2 f/c biomicroscope optical setup

The optical system schematic is presented in Fig. 1. We used a fiber-coupled Ar/Kr ion laser and a diffraction grating to select the 488 nm spectral line as the excitation source. At the fiber output, the beam was collimated to be approximately 3.5 mm in diameter. The first element was the segmented MEMS deformable mirror (DM) with modal control and a 5 µm stroke (PTT111, Iris AO, Inc, Berkeley, CA), which also defined the first pupil plane. Two lenses, f_1 = 200 mm and f_2 = 200 mm, relayed the conjugate plane to the tunable liquid lens (Varioptics, Arctic 39N0) for focus control and for optical sectioning of the different retinal layers. Relay lenses with focal lengths of f_3 = 150 mm, and f_4 = 100 mm were used to decrease the beam's diameter and to relay the pupil to the scanning mirrors. The beam position was scanned over the sample with two 6210H galvanometer mounted mirrors (Cambridge Technology Inc.) for each direction. Next, two lenses, f_5 = 25 mm, and f_6 = 75 mm expanded the beam's diameter and relayed the pupil to the final objective lens. The beam was focused with a NA = 0.17 to a final spot (Gaussian waist) of 0.9 µm and the axial point spread function was 38 µm with a Mitutoyo infinity-corrected long working distance 10x objective lens. The backscattered light (reflectance) was coupled into a 100 µm multimode fiber (3.9 Airy disks in diameter) and detected by an Avalanche Photo Diode (APD, Hamamatsu S5343). We also used a quarter-wave plate (QWP) to act on the linearly polarized light from the laser and a linear analyzer at the detector to reduce the specular reflection from the optical elements [16]. The backward-directed fluorescence signal was isolated by a dichroic mirror and a long-pass filter (Semrock 496 nm blocking edge BrightLine, FF01-496/LP-25). The fluorescence light was focused by an 80 mm lens through a 50 µm confocal pinhole with diameter 1.8 times the size of the Airy disk, and a Photo-Multiplier Tube (PMT, Hamamatsu H7827-002) was used to detect the weak fluorescence signal. An analog-to-digital converter digitized the signal from the APD and PMT simultaneously, and the imaging system speed was limited to 1.00 Mega-Samples Per Second (MSPS) per channel by the NI PCIe-6361. The galvanometers were driven by a 1 kHz sinusoidal waveform scanning pattern, and acquired data from both forward and backward sweeps of the scan. Image distortion caused by the non-linear scanning pattern was corrected with de-warping in real-time using custom software developed in C/C + + for acquisition and display. This allowed for 400x400 reflectance and fluorescence samples per frame at 5 fps, which was used for aligning the mouse eye and for data streaming. The AO optimization was performed at 400x100 samples which corresponded to an acquisition and display rate of 20 fps. The icon of a computer in Fig. 1 has representative images for each channel displayed during imaging.

#246171 Received 30 Jul 2015; revised 15 Oct 2015; accepted 21 Oct 2015; published 4 Dec 2015

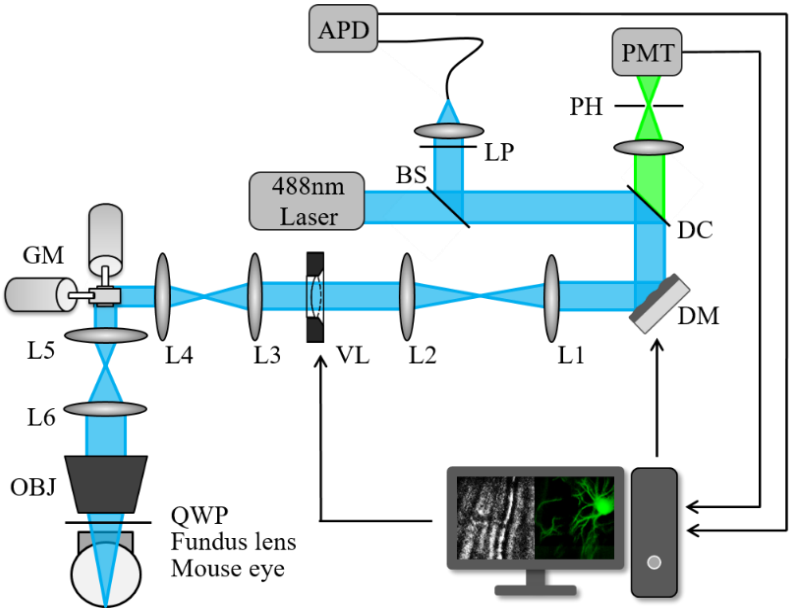

Fig. 1. Schematic of the WSAO f/c biomicroscope using 488 nm excitation from an Ar/Kr laser. Relay lenses are achromatic doublets. Other optical elements: 80/20 beam splitter (BS), dichroic mirror (DC), deformable mirror (DM), zero-order quarter wave plate (QWP), objective lens (OBJ), linear polarizer (LP), pinhole (PH), variable lens (VL), galvanometer scanning mirrors (GM). Electronic elements: avalanche photo diode (APD), photo multiplier tube (PMT). The images on the computer icon are representative images of the structural and fluorescence imaging channels.

2.3 Image acquisition and optimization

The anesthetized mouse was placed in front of the fundus lens to initiate imaging. The retinal imaging location was determined based on landmarks such as the vascular pattern and the optic nerve head. The maximum FOV on the mouse retina was ~0.8 mm with the mouse cornea approximately perpendicular to optical axis of the system. The position of the fundus lens was fixed in the center of the optical path, and different eccentricities on the mouse retina were imaged by rotating the orientation of the mouse with respect to the fundus lens. The focus was adjusted using the Varioptic lens in order to get the best qualitative image appearance [27].

The WSAO optimization algorithm that we used is a modified version from our previous report for WSAO mouse imaging with OCT [21]. During optimization, the frame rate of the WSAO f/c biomicroscope presented in this report was 20 fps with a frame size of 400x100 samples. Following optimization, higher quality images were acquired with 400x400 samples per frame at 5 fps. The optimization algorithm used a modal control to build up an optimal shape of the DM that corrected for the wavefront aberrations. For each Zernike mode, the algorithm searched through 21 coefficient values; the search range for a particular Zernike mode was selected from typical aberration amplitudes for mouse eyes. A larger range was searched for lower order aberrations and a smaller range for higher order aberrations. We were able to correct for up to the 20th Zernike mode (OSA convention [28]) in ~30 seconds.

The WSAO used a hill-climbing search algorithm to find the best set of Zernike coefficients that corrected for aberrations based on the image quality metric. The overall intensity of an image was calculated as the sum of each pixel, defining the merit function $J(k)$ as in Eq. (1):

#246171 Received 30 Jul 2015; revised 15 Oct 2015; accepted 21 Oct 2015; published 4 Dec 2015

$$J(\mathbf{k}) = \sum_{x,y} \mathrm{I}_{w(\boldsymbol{k})}(x, y), \tag{1}$$

where **k** is a vector of Zernike coefficients and $\mathrm{I}_{w(\mathbf{k})}$ is the acquired intensity if the pixel at the image coordinates *x*, *y*. The wavefront shape, $w(\mathbf{k})$, applied to the DM is given by Eq. (2):

$$w(\mathbf{k}) = \sum_{n=3}^{20} k_n Z_n. \tag{2}$$

The flowchart in Fig. 2 is a summary of the optimization process. The algorithm applied a linearly spaced range of coefficients (k_n) for each Zernike mode (Z_n) to the DM and recorded an image for each pre-set coefficient value. The optimal image, and thus the optimal coefficient value, was determined as the one that corresponded to the highest value of the merit function. The optimization began with defocus (n = 4) [28] and first three Zernike modes (piston, tip and tilt) were assigned a coefficient value of zero and not included as part of the optimization. The Zernike modes were optimized in the order as presented on the abscissa of Fig. 6(b).

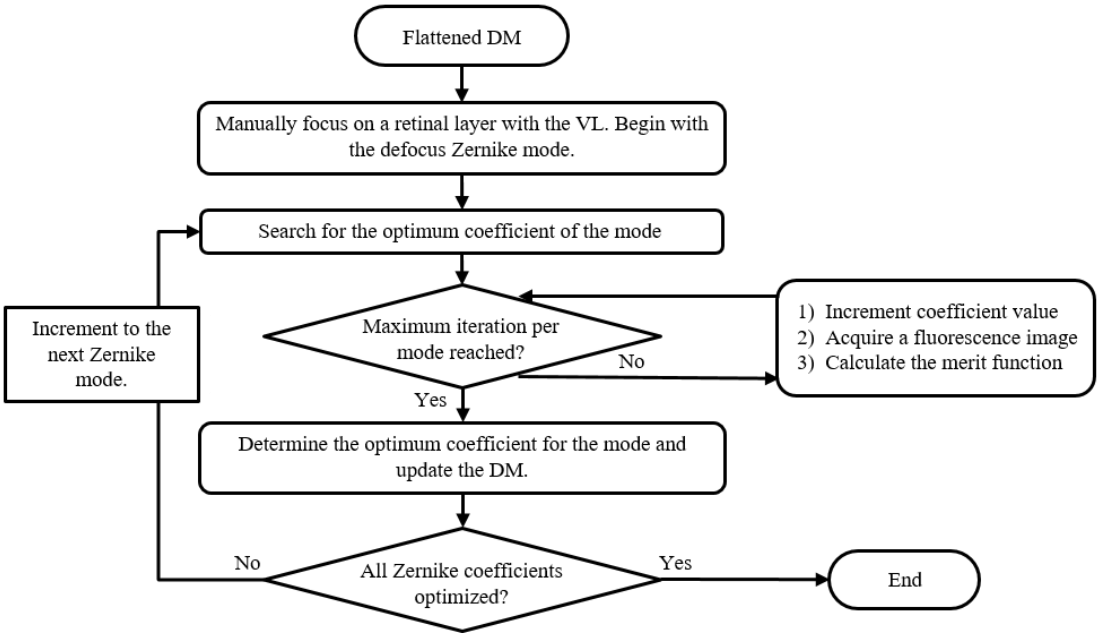

Fig. 2. WSAO modal hill-climbing algorithm flowchart for the fluorescence image optimization process; deformable mirror (DM), variable lens (VL).

3. Results

3.2 WSAO f/c biomicroscope resolution

The biomicroscope system design was computer simulated with Zemax (ZEMAX Development Corporation, Bellevue, WA) to model the spot size on the mouse retina off of the optical axis. The simulation results predicted diffraction-limited performance within a 0.2 mm FOV. The FOV on the retina was limited to ~0.8 mm by lens L6 in Fig. 1; note that this imaging mode was not diffraction limited, but useful for navigation to landmarks on the retina.

The performance of the optical imaging system was evaluated for both reflectance and fluorescence channels on resolution targets. The performance of the reflectance imaging

#246171 Received 30 Jul 2015; revised 15 Oct 2015; accepted 21 Oct 2015; published 4 Dec 2015

system was measured by setting the DM to the flat position and placing a US Air Force (USAF) resolution target (Fig. 3) in the retinal plane. We imaged groups 6 and 7 of the USAF target and we were able to resolve the smallest element of group 7 that has a line width of 2.19 µm.

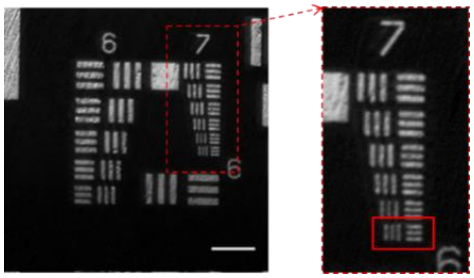

Fig. 3. US Air Force resolution target with line width 2.19 µm highlighted by the red rectangle to demonstrate the reflectance resolution. Scale bar: 50 µm.

The resolution of the fluorescence channel was measured by imaging fluorescent beads (190508, Polyscience, Inc.) that had a diameter of 2.1 µm with a standard deviation of 0.018 µm. The WSAO optimization was performed on the fluorescent signal from the beads and the intensity profile across the diameter of a representative bead was plotted to demonstrate the system resolution and AO performance (Fig. 4). A line plot of a bead after optimization shows a 5% intensity increase and a narrower full width at half maximum, suggesting that the optimization corrected small system aberrations. The RMS of the Zernike polynomial coefficients obtained from this optimization was 0.02 µm, which is below the Maréchal criterion for diffraction-limited imaging ($\lambda/14$).

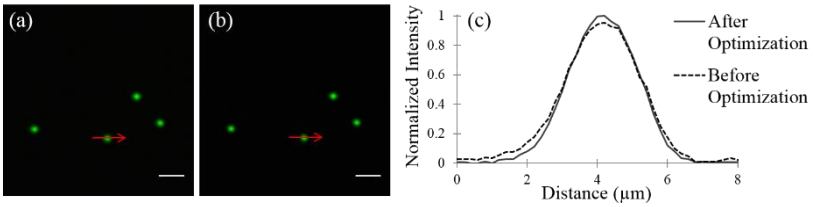

Fig. 4. Images of 2.1 µm diameter fluorescent beads acquired a) before WSAO optimization and b) after optimization. c) The line plots for a bead before and after optimization. Scale bars: 10 µm.

3.3 In vivo WSAO confocal fluorescence imaging of retinal ganglion cells

We acquired retinal images of anesthetized mice to demonstrate the WSAO f/c biomicroscope performance *in vivo*. Images of an EGFP-labelled ganglion cell are displayed before and after the optimization in Fig. 5. A video of the change in the appearance of the ganglion cell during the optimization process as displayed on the screen is included in Visualization 1. The images in Fig. 5 were produced using identical processing steps, and by averaging 50 registered frames. The Medical Image Registration Toolbox (MIRT) for Matlab was used to register the frames prior to averaging [29]. Given the small amplitude and slow speed of intra-frame motion in the anesthetized mice during the 5 frames per second acquisition, we used a non-rigid cubic B-spline registration algorithm with a sum of squared differences similarity metric. In the presence of larger amplitude or faster motions, more advanced registration algorithms, for example strip-based registration [30–32], may achieve better performance. The intensity-based similarity measurement performed well for the frames with a strong signal from Fig. 5(b), although the registration was less effective for the dendrites in Fig. 5(a) due to the lower signal intensity. The dendrites in Fig. 5(b) appear to be less resolved on the right side of the image; this is due to the dendrites being out of the focal plane. The optimization results for

#246171 Received 30 Jul 2015; revised 15 Oct 2015; accepted 21 Oct 2015; published 4 Dec 2015

these images are plotted in two ways: the optimum Zernike coefficient value determined by the search algorithm (Fig. 6(a)) and the corresponding merit function for each optimized mode in the order of the optimization (Fig. 6(b)). The intensity profile of a dendrite is displayed in Fig. 6(c) to demonstrate the AO performance. Ganglion cells are classified into types based on the cell structure with properties including soma size and dendrite patterns; a short review of this topic was presented in Geng *et al.* [1]. The image of the ganglion cell in Fig. 5 appears to have a round soma that is approximately 20 μm in diameter with thick and straight dendrites. Based on this description, this ganglion cell may belong to the RG_{A2} category as described by Sun *et al.* [33]. This classification is further supported with the description by Coombs *et al*. [34] and images by Geng *et al.* [1].

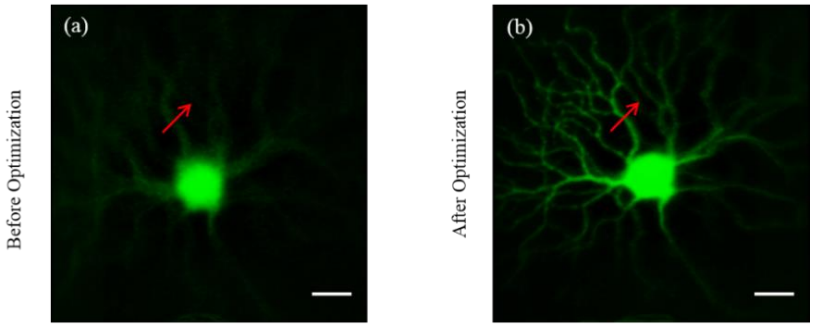

Fig. 5. a,b) Ganglion cells labelled by EGFP comparing the images acquired before and after the WSAO optimization. These images are an average of 50 frames of an off-axis ganglion cell. Scale bars: 20 μm.

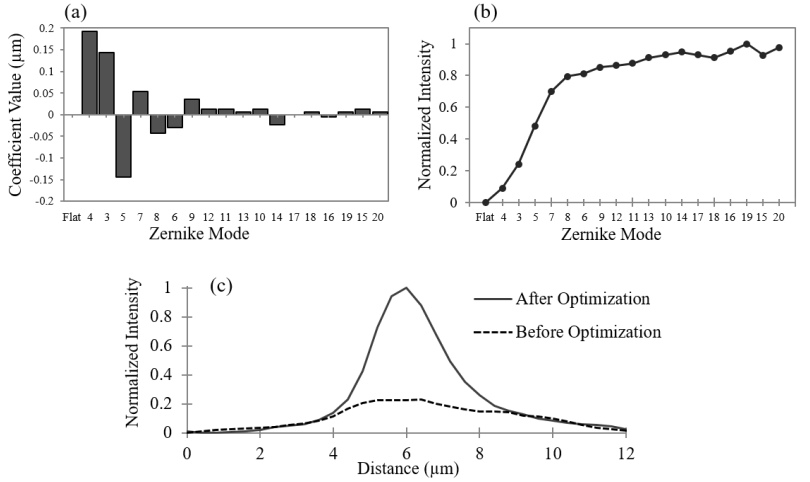

Fig. 6. a) The Zernike coefficients applied to the DM (deformable mirror) after the optimization. b) The impact of the optimization on the intensity-based merit function are plotted for each mode. The intensity is normalized from zero when the DM is flat. The Zernike coefficients are reported by the OSA standard for optical aberrations of eyes [28]. c) The intensity plot of a dendrite on the EGFP-labelled ganglion cell at the location and in the direction indicated by the arrows.

3.4 In vivo WSAO confocal fluorescence imaging of retinal microglia cells

We also imaged EGFP-labelled microglia cells with similar results. The images of microglia presented in Fig. 7 before and after the optimization were processed by the same method as the ganglion cell images. In Fig. 7(b) the fluorescence signal on the left side of the image has lower intensity after the optimization due to the microglia being at a different depths within

#246171 Received 30 Jul 2015; revised 15 Oct 2015; accepted 21 Oct 2015; published 4 Dec 2015

the retina. This demonstrates the optical axial sectioning effects of the confocal pinhole and the ability of WSAO to reject out-of-focus features.

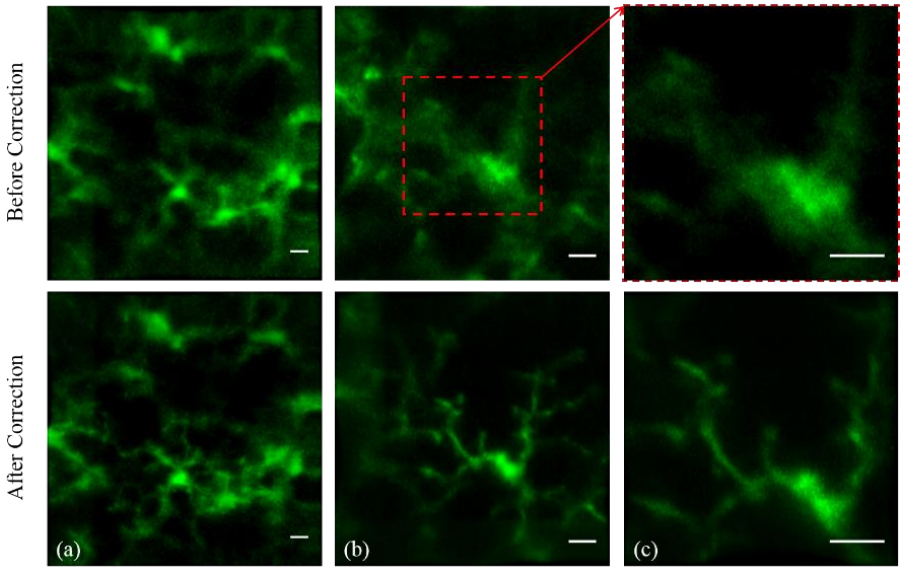

Fig. 7. Images of EGFP-labelled retinal microglia cells acquired *in vivo* before and after WSAO correction with different field of views: a, b, and c. Images b) and c) were taken at the same location with different field of views as indicated by the red dashed box. Each image is an average of 50 frames. Scale bars: 10 µm.

4. Discussion

The mouse eye is commonly used as a model of the human eye for vision research. High quality images of the retina can be acquired without AO in some mice, in particular for animals with healthy eyes [5, 6]. Time course studies in mice and research on transgenic mouse models of degenerative retinal diseases stand to benefit from the incorporation of AO with the imaging system for increased resolution across a wider range of animals, improved consistency in image resolution between time points, and for locations that are off the optical axis of the eye. Additionally, AO provides the ability to control the focus plane of the imaging system, which allows for easy and controlled transition between layers of interest within the retina. Developing accessible AO that is low-cost and small in size has the potential to be more widely used across multiple research specialties.

We demonstrated WSAO for non-invasive *in vivo* fluorescence imaging of the mouse retina. Our results showed cellular-resolution images acquired using a lens-based AO system without the difficulties associated with implementing a WFS for mouse retinal imaging. Our system included two electronically controllable elements on optically conjugated pupil planes: a tunable lens controlling defocus for layer selection (which can loosely be referred to as a 'woofer') and a deformable mirror for higher order corrections ('tweeter') [35–37]. We used an intensity-based image quality metric to search for the Zernike coefficients that would produce the strongest fluorescent signal and hence better resolution. Recent research results suggest that using an intensity-based metric exclusively is not sufficient for confocal scanning ophthalmoscopes, due to differences in the illumination and the collection paths. Sulai *et al*. have demonstrated an approach using a sharpness metric to optimize the point spread function of the illumination path in order to increase the resolution [14]. In future work, we will investigate the use of a sharpness metric, for example as defined in [14], in place of the intensity metric used in this work. We anticipate that in cases where the fluorescent signal

#246171 Received 30 Jul 2015; revised 15 Oct 2015; accepted 21 Oct 2015; published 4 Dec 2015

arises from non-planar structures that a sharpness metric will result in an improved optimization performance.

The WSAO f/cSLO method used the same source of light (the fluorescence) confined to a single retinal layer for both imaging and for guiding the aberration correction (since the merit function was derived from the fluorescence images). In common AO imaging configurations using a SH-WFS, the sensing ('beacon') and imaging wavelengths are different. According to Zhou *et al.* [38], the chromatic defocus between the sensing light and the imaging light are significant in the small animal eye, and can introduce higher order aberrations in addition to defocus. This further accents a strength of the WSAO technique, in that the aberration correction is performed at the same retinal depth section that is being imaged, for example with the ganglion cells in the inner retina.

Our optimization algorithm required ~30 seconds to perform an exhaustive search up to the 20th Zernike mode with 21 steps per mode. In addition to the modal hill-climbing algorithm demonstrated in this paper, the performance of other approaches such as the simulated annealing algorithm or the stochastic parallel gradient descent algorithm could also be explored [39, 40]. For human imaging, the WSAO optimization speed is essential due to the motion of the patient [21]. However, for an anesthetised mouse the amount of motion is low and the optimization speed is not as crucial; this is supported by a recent report by Palczewska *et al.* [41], where they used WSAO for two-photon microscopy and required 4-6 minutes for an optimization.

The approach to WSAO retinal imaging in mice described in this report utilized a fixed microscope objective lens and a plano-concave lens with radius of curvature matched approximately to the curvature of the eye, reducing the refraction at the cornea. This configuration constrained the FOV by the size of the mouse pupil and the mismatch between the field curvature at the image plane of the objective lens and the curvature of the mouse retina. Delivering a collimated beam into the mouse eye and allowing the cornea and lens to focus it on the retina would provide a larger FOV. However, with a collimated beam approach, a significantly larger amount of focus correction would be required to optically section through the retina, on the order of ~30 – 40 diopters [7]. Another possible solution for our system would be to design a custom multi-element objective lens with a scan pivot closer to the pupil in order to permit a wider field of view. An advantage of this approach is in the potential ease of reconfiguring the system for AO retinal imaging in different animal species, such as rats (see recent work by Geng *et al.* [42]). This would require only a change in the final objective lens to accommodate a different NA and the final concave surface to accommodate a different corneal curvature.

A significant benefit of the WSAO algorithm is that the aberration correction is less sensitive to multiple reflections from the sample and optical elements. Even in the presence of undesired reflections that would affect SH-WFS wavefront measurement, WSAO could still perform the optimization if these reflections do not change significantly with the DM shape or if they are removed from the region of interest used for the merit function with image processing techniques. As reported by Biss *et al.* [22] and Geng *et al.* [7], challenges in wavefront sensing can arise due to reflections from different layers within the relatively thick mouse retina as well as due to increased scattering. This effect is even more pronounced in albino animals, in which the choroid and sclera layers also generate a large backscattered signal. We employed a confocal detection which allowed the WSAO to optimize the image signal within the depth of focus and minimize the out of focus signal. The mice used for imaging in this report were pigmented; however, since the WSAO algorithm does not rely on wavefront sensing, identical performance is anticipated in non-pigmented animals. We have recently demonstrated WSAO OCT in albino mice with no difference in performance with respect to pigmented mice [43].

#246171 Received 30 Jul 2015; revised 15 Oct 2015; accepted 21 Oct 2015; published 4 Dec 2015

5. Conclusion

In this report, we demonstrated WSAO for non-invasive *in vivo* fluorescence imaging of the mouse retina. We imaged transgenic mice with EGFP-labelled ganglion and microglia cells and used WSAO to increase the image resolution by correcting for wavefront aberrations introduced by the eye. The AO system demonstrated cellular-resolution imaging with a low-cost, simple and robust lens-based system. The future applications of WSAO would enable high-resolution longitudinal studies with fluorescence images.

Acknowledgments

We acknowledge funding for this research from Canadian Institutes of Health Research, Natural Sciences and Engineering Research Council of Canada, Michael Smith Foundation of Heath Research, Alzheimer Society Research Program, and Pacific Alzheimer Research Foundation. R.J. Zawadzki was supported by the National Eye Institute UC Davis Vision Center Core Grant (P30EY012576), UC Davis Research Investments in Science and Engineering (RISE) Grant, and NSF I/UCRC CBSS Grant.